

# We are IntechOpen, the world's leading publisher of Open Access books Built by scientists, for scientists

4,800

Open access books available

122,000

International authors and editors

135M

Downloads

Our authors are among the

154

Countries delivered to

TOP 1%

most cited scientists

12.2%

Contributors from top 500 universities



WEB OF SCIENCE™

Selection of our books indexed in the Book Citation Index  
in Web of Science™ Core Collection (BKCI)

Interested in publishing with us?  
Contact [book.department@intechopen.com](mailto:book.department@intechopen.com)

Numbers displayed above are based on latest data collected.  
For more information visit [www.intechopen.com](http://www.intechopen.com)



# Catalyst Characterization with FESEM/EDX by the Example of Silver-Catalyzed Epoxidation of 1,3-Butadiene

Thomas N. Otto, Wilhelm Habicht,  
Eckhard Dinjus and Michael Zimmermann  
*Karlsruhe Institute of Technology, IKFT,  
Germany*

## 1. Introduction

Ag catalysts are of outstanding importance in the field of heterogeneous catalysis. Optimum distribution and morphology of the Ag particles must be ensured by controlled, tailored catalyst synthesis. Hence, there is a growing demand for the characterization of Ag-dispersed fine particle systems requiring high-resolution surface observation of particles down to a few tens of nanometers and elemental analysis by *field emission scanning electron microscopy and energy-dispersive X-ray spectrometry* (FESEM/EDX). It is beneficial to characterize the particle morphology by comparison of different imaging methods like secondary electron (SE)-, backscattered electron (BSE)- and transmitted electron (TE) detection. In scanning electron microscopy surface topography becomes visible due to the dependency of the SE yield on the angle of electron incidence. Together with the large depth of field informative images of irregularly shaped particle structures are obtained. The increased BSE yield of high atomic numbers ( $Z$ ) such as Ag catalysts and promoters (e.g. Cs) compared to a low-density matrix and the high penetration depth of 20-30 keV electrons also allows imaging and analysis of inclusions that would be obscured at low beam energies. Both SE and BSE detectors, in particular at low beam voltages, can additionally reveal interesting surface features of fine Ag particles. A well-known example for a Ag catalyzed reaction is the  $\alpha$ - $\text{Al}_2\text{O}_3$  supported Ag-catalyzed epoxidation of 1,3-butadiene to 3,4-epoxybutene. The electrophilic addition of oxygen across the carbon-carbon double bond of 1,3-butadiene, resulting in a three-member ring structure that can undergo further chemical transformations to oxygenated products, such as ketones, alcohols, and ethers. Supported silver catalysts have been shown to epoxidize olefins with nonallylic hydrogen when an alkali promoter is doped on the surface. Thus, the direct kinetically controlled oxidation to the corresponding epoxide is preferred. The guiding hypothesis for this partially oxidation is that surface oxametallacycles are key intermediates for epoxidation on promoted Ag catalysts. Therefore, the preparative application of Ag and promoters (Cs, Ba) on the catalyst support material is of great importance. Another important aspect is sintering of Ag particles which may reduce the catalytically active surface and decreases the overall reaction performance. For this research, catalysts are produced by sequential impregnation of two mineralogically differing support materials (SC13, SLA2) with an

aqueous active component solution ( $\text{AgNO}_3$ ,  $\text{CsNO}_3$ ). The two selected Ag catalyst systems are examined using mainly FESEM/EDX. The determination of metal amount were carried out with EDX area analysis and, if necessary, supplemented by EDX-spot analysis. In some cases, characterization of Ag-distributions by EDX mappings were made. Furthermore, for the Monte Carlo (MC)- simulations x-ray line scans of two different SEM preparation techniques (bulk specimen, thin-film supported specimen) were performed to underpin the relationships impressively. Temperature-programmed  $\text{O}_2$  desorption ( $\text{O}_2$ -TPD) as well as  $\text{N}_2$  sorption (BET) measurements are important analysis methods in catalysis chemistry, too. Both methods are used to support the FESEM/EDX investigation to provide complementary contributions with regard to the Ag distribution and the properties of the carrier surfaces.

## 2. Characterization and measurement methods

### 2.1 Ag catalyst systems

Huge varieties of materials are used in the preparation of heterogeneous catalysts, especially industrial catalysts. Catalysts can be divided into three groups of constituents, namely active catalytic agents, promoters, and supports [1]. Catalysts are manufactured by various methods, such as wet impregnation, leaching, drying and calcination. The major components of the catalyst system are the catalyst support (bulk material, e.g.  $\text{Al}_2\text{O}_3$ ,  $\text{TiO}_2$ ,  $\text{SiO}_2$ ), which might influence the catalytic activity of the active components (metal-support interactions, MSI) [2] and the active metal e.g. Ag, Pd, Pt is the active agent. Increasing the surface area of the active agent is one function of the support. Maintaining a high dispersion of the active components is the other function.  $\alpha$ - $\text{Al}_2\text{O}_3$  with its small specific surface area has proved to be a wear-resistant carrier material for Ag and to be highly suited for the selective oxidation of 1,3-butadiene [3].

### 2.2 Catalyst preparation

The Ag catalysts for this research are produced by sequential incipient wetness impregnation of two mineralogically different carrier materials with an aqueous solution of  $\text{AgNO}_3$  and  $\text{CsNO}_3$  as active components. The following catalyst supports are applied:

- SC13 (Almatis) mineralogical: 80 %  $\alpha$ - $\text{Al}_2\text{O}_3$ , 20 %  $\gamma$ - $\text{Al}_2\text{O}_3$ , Chemical composition: 99 %  $\text{Al}_2\text{O}_3$ , 0.05 %  $\text{CaO}$ , 0.03 %  $\text{Fe}_2\text{O}_3$ , 0.02%  $\text{SiO}_2$ , 0.4 %  $\text{Na}_2\text{O}$ .
- SLA92 (Almatis) mineralogical: Main phase Ca hexa aluminate (CA6) hibonite, secondary phase  $\alpha$ - $\text{Al}_2\text{O}_3$ , chemical composition: 91%  $\text{Al}_2\text{O}_3$ , 8.5 %  $\text{CaO}$ , 0.04 %  $\text{Fe}_2\text{O}_3$ , 0.07 %  $\text{SiO}_2$ , 0.4 %  $\text{Na}_2\text{O}$ .

Dry SC13 and SLA92 are pre-sieved and subjected to wet sieving (Retsch laboratory sieves manufactured according to DIN 3310, mesh width 0.045 mm – 0.063 mm). The sieve fractions are dried at 120°C in a circulating air oven for 5 h. The desired active component solutions  $\text{AgNO}_3(\text{aq})$  and  $\text{CsNO}_3(\text{aq})$  are applied sequentially to the carrier materials and subjected to an ultrasound bath for 0.5 min (Sonorex RK 100H) [4]. The precursors are dried in a circulating air oven at 40°C for 5 h and then oxidized with 100 %  $\text{O}_2$  (4.8) at 250 °C for 10 min ( $4000 \text{ ml}_{\text{STP}} \text{ h}^{-1}$ ). A reduction with 100 %  $\text{H}_2$  (6.0) follows at 200 °C for 10 min ( $1000 \text{ ml}_{\text{STP}} \text{ h}^{-1}$ ). The concentrations of the active metal (oxidation number  $\pm 0$ ) components after conditioning are given by:

D1, SC13, 45/63 $\mu\text{m}$ , 5 % Ag	MZ06, SLA 92, 45/63 $\mu\text{m}$ , 5 % Ag, 1500 ppm Cs
D2, SC13, 45/63 $\mu\text{m}$ , 5 % Ag, 1500 ppm Cs	MZ09, SLA 92, 45/63 $\mu\text{m}$ , 10 % Ag, 1500 ppm Cs
D3, SC13, 45/63 $\mu\text{m}$ , 10 % Ag	
D4, SC13, 45/63 $\mu\text{m}$ , 10 % Ag, 1500 ppm Cs	
D5, SC13, 45/63 $\mu\text{m}$ , 20 % Ag	
D6, SC13, 45/63 $\mu\text{m}$ , 20 % Ag, 1500 ppm Cs	

### 2.3 Electron interactions with the specimen

Scanning electron microscopy in combination with energy-dispersive X-ray spectrometry (SEM/EDX) is a well-established and versatile method for the characterization of heterogeneous catalysts, especially Ag catalysts. They are predominantly composed of small metal particles dispersed onto a supporting material, generally a chemically inert oxide. Information about particle size distribution, deposition on the substrate surface, and elemental compositions can be obtained easily. In FESEM, a high brightness Schottky-type field emission (FE) cathode with its small beam diameter (spot size) enables imaging of features with high resolution and high contrast down to the nanoscale even on bulk substrates. Coincidentally, the element composition of the specimen is available by excitation of inner shell electrons to collect characteristic X-rays with sufficient intensity for analytical information. Due to the high depth of field ( $D \approx d^2 / \lambda$ ,  $\lambda_{20 \text{ keV}} = 0.0086 \text{ nm}$ ), where  $D$  is the depth of field,  $d$  is the apparent resolution, and  $\lambda$  is the electron wavelength, impressive images of differently shaped catalyst particles can be generated [5]. In the SEM, the primary electron beam creates different types of electron interactions, while penetrating the specimen. For this research, however, we utilize the following 4 important electron interactions with the specimen, namely the generation of

- secondary electrons (SE)
- backscattered electrons (BSE)
- transmitted electrons (TE)
- characteristic X-rays

Secondary and backscattered electrons are essentially for the topographical imaging of the specimen surface and therefore are described in more detail in chapter 2.4. Transmitted electrons (TE) interact less with the specimen. The specimen appears more or less "transparent" for electrons, depending on the *thickness and density* of the specimen. In energy-dispersive X-ray Spectroscopy (EDX), the X-rays are produced by inelastic scattering of primary beam electrons with bound inner shell electrons during their penetration into the matter. Subsequent deexcitation by transition of outer shell electrons to the inner shell vacancy results in emission of an element specific X-ray quantum [6]. These characteristic X-rays are essential for the determination of the elemental composition of a specimen. The electron penetration depth depends mainly on the primary beam energy and the target composition. The X-ray production range also depends on the critical excitation energy of the specific X-ray line (e.g.  $K\alpha$  or  $L\alpha$ ) and is always smaller than the electron range. The electron range is the travelling distance from the primary beam electron incident at the target surface to the point where the electrons lost their energy by multiple interaction processes within the material. Figure 1 illustrates the different kinds of electron interactions with specimen and the according electron detectors.

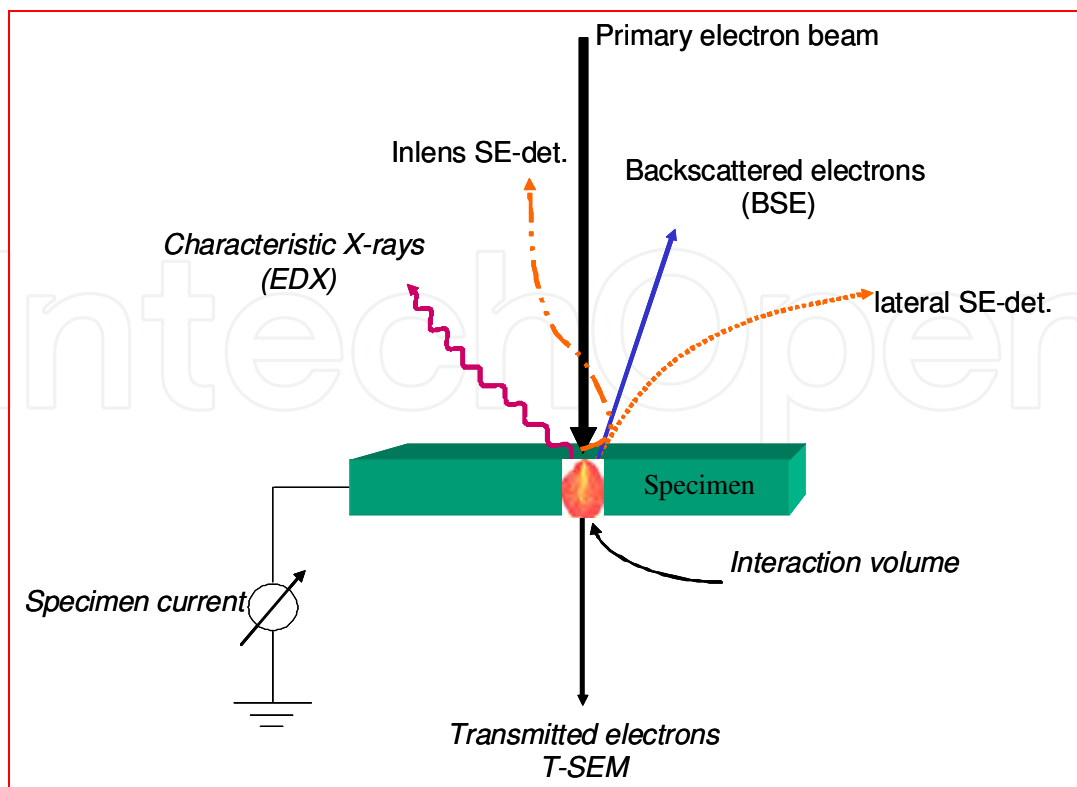


Fig. 1. Different types of electron interactions with specimen and related detection modes.

## 2.4 Imaging modes

Secondary electrons (SE), backscattered electrons (BSE) and transmitted electrons (TE) are responsible for three different imaging modes in SEM. The fourth type of electron interaction is the generation of X-rays and, hence, not a typical imaging mode.

The 3 imaging modes are explained as follows:

1. Backscattered electrons provide contrast based on atomic number ( $Z$ -contrast) and density. The BSE-detector will be used as a quick response to visualize materials heterogeneously composed and distributed. It will be applied often in combination with the EDX- unit to capture images for subsequent microanalysis. Depending on the primary beam energy, backscattered electrons are created inside the specimen by elastic scattering. They possess approximately the energy of the primary electrons. As a rule of thumb, the exit depth of the BSE is half the primary electron range. As a consequence, the imaging resolution achieved by backscattered electrons is worse than those achievable by secondary electrons.
2. Low energetic ( $< 50$  eV) secondary electrons are used for true surface imaging, because they are created in the vicinity of the primary beam impact on the target surface. They are responsible for high-resolution imaging (in-lens SE detection).
3. Transmission-type images (also called T-SEM mode) are obtained by a special mounting device for TEM grids with a diode-type detector beneath. The detector is mounted like a specimen stub instead and also adjusted to the electron beam. The specimen must be sufficiently thin ( $< 200$  nm) to permit penetration of beam electrons at 20-30 kV, which is the typical operation voltage in T-SEM mode. Imaging of mass-

thickness contrast is enabled. The application of the TE- detector can provide additional information on the sub-surface structure of many particles which cannot be resolved clearly in the corresponding SE and BSE images. The thin-film-supported specimen permits imaging with enhanced contrast due to an improved signal-to-noise ratio and X-ray analysis with reduced scattering background [7], [8].

## 2.5 Specimen preparation for SEM / T-SEM

The specimens are fixed with conductive tabs onto Al-stubs as bulk specimen for conventional SEM imaging. For T-SEM imaging, the samples are suspended in ethanol, and a droplet is poured onto a carbon-film-coated TEM-grid (400 meshes Cu, ca. 8 nm C) for transmitted electron measurements.

## 2.6 SEM equipment

The electron microscopic investigations are carried out with a DSM 982 Gemini, Zeiss corp., Germany, equipped with a 4-quadrant solid-state BSE detector, a high brightness in-lens SE detector and a lateral SE detector. The DSM 982 GEMINI is applied with a thermal (Schottky-type) field-emission electron source (SFE). Element-specific quantification is performed by the dedicated EDX unit, equipped with a 30 mm<sup>2</sup> Si(Li) detector INCA Pentafet™, FWHM 129 eV @ MnK $\alpha$  (Oxford corp., England).

## 2.7 O<sub>2</sub>-TPD

O<sub>2</sub>-TPD analysis is performed using a BELCAT-B (BEL INC. Japan) system. It is coupled with a GAM 400 quadrupole mass spectrometer (In Process Instruments, Germany) as a mass-selective detector. The samples are subjected to a preliminary in-situ treatment in an O<sub>2</sub> / He test gas mixture. For this purpose, the sample is heated to 250°C in steps of 5 K/min and then kept at 250°C for 1 h. After this, it is cooled down to room temperature (RT). At RT, the non-adsorbed O<sub>2</sub> is removed by rinsing with He. In the subsequent O<sub>2</sub>-TPD experiment the pre-treated samples are heated linearly in He. A thermal conductivity detector (WLD) is applied. The quadrupole mass spectrometer determines the composition of the desorbed products.

## 2.8 N<sub>2</sub>-BET

The BET surface area (S. Brunauer, P. H. Emmett, and E. Teller) is determined with N<sub>2</sub> (77 K) (BELSORP-mini II, BEL INC. Japan). All samples are subjected to a preliminary treatment in a vacuum at 200°C for 5 h. To determine the sorption isotherms, the amount of molecules adsorbed on the samples are measured as a function of the relative pressure  $p/p_0$ . The specific surfaces are calculated from the adsorption parts of the isotherms at 77 K in the relative pressure range from 0.01 to 0.35  $p/p_0$  with N<sub>2</sub>.

## 3. Discussion

### 3.1 Electron microscopy affecting parameters and MC simulation

FESEM and the dedicated EDX unit are important aids in the determination of the relationship among catalyst particle (cluster) sizes, dispersion onto support, support



morphology and the influence of promoters. For a better understanding it makes sense to calculate the practical electron range by the Monte Carlo simulation program MOCASIM™ [9]. Additionally, the depth of the X-ray generating region (X-ray range) is estimated for the materials under consideration. It is based on an analytical expression useful for most elements and is calculated by the equation 1 of Andersen-Hasler:

$$R = \frac{0.064}{\rho} \cdot (E_0^{1.68} - E_c^{1.68}) \quad (1)$$

Whereby R (μm) is the X-ray range, E<sub>0</sub> (keV) is the primary electron (beam) energy, E<sub>c</sub> (keV) is the critical excitation energy for the characteristic (analytical) X-ray line and ρ is the density of the elements. The dimension of the primary X-ray generation volume is important for the information depth obtained. It depends on the beam energy and the X-ray line chosen for the measurement [10]. The dependency of the practical electron range (penetration depth) and the X-ray range on the material density and beam voltage (beam energy) of the catalyst materials Ag, Al, and Al<sub>2</sub>O<sub>3</sub> is depicted in Tab. 1. The higher the density of the element or specimen, the less is the penetration depth of the electrons (practical electron range) and the X-ray range (information depth). As a consequence, the material should be ideally homogeneous over the electron range to minimize errors caused by specimen heterogeneity. The critical excitation energy is determined by the specific absorption edge for the electron shell of an element from which the analytical X-ray line will be emitted. Therefore, E<sub>c</sub> is always slightly higher than the corresponding X-ray line.

Specimen	ρ / g cm <sup>-3</sup>	X-ray line / keV	E <sub>c</sub> / keV	HV / kV	pract. Electron range / nm	X-ray range / nm
Al	2.7	1.487 (Kα)	1.56	5	361	304
				10	1146	1085
				15	2252	2192
				20	3639	3585
Al <sub>2</sub> O <sub>3</sub>	3.5	-	-	5	278	235
				10	884	837
				15	1738	1691
				20	2807	2766
Ag	10.5	2.984 (Lα1,2)	3.35	5	93	45
				10	295	245
				15	579	530
				20	936	888

Table 1. Parameters affecting the electron range and X-ray range. E<sub>c</sub> is the critical excitation energy for the corresponding analytical X-ray line. The practical (pract.) electron range is calculated by MOCASIM™.

The different penetration depths for heterogeneously composed materials will be overcome by using the T-SEM technique as it will be discussed later. As depicted in Figure 2 and Figure 3 the MC simulations elucidate the different excitation volumes for 5 keV and 20 keV beam energies. They interact with an Alox ( $\text{Al}_2\text{O}_3$ ) support covered with an Ag cluster that is assumed to be 100 nm in thickness. It demonstrates the differences in the electron ranges as a function of beam energies and material density whereas the relative atomic number Ag (107.8) and the relative molecular weight  $\text{Al}_2\text{O}_3$  (101.9) are close together. Remarkable is the beam spreading effect caused by multiple scattering in the bulk specimen, which leads to a pear-like shape of the electron trajectories (interaction volume). This will be drastically reduced by using thin supporting foils and thinning of the specimen or using sufficiently small particles, depending on the beam voltage and density of the specimen (see Figure 10).

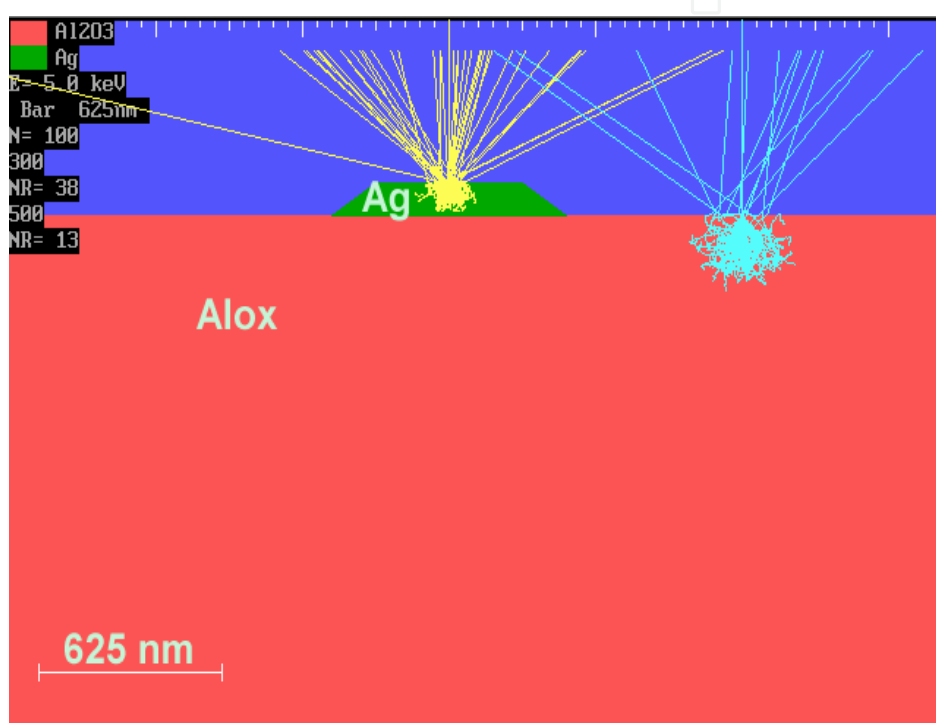


Fig. 2. MC simulation of electron trajectories (interaction volumes) created by primary beam energy of 5 keV. Note that N is equal to the number of used trajectories (100) for MC simulation. NR corresponds to the number of BS-electrons in case of Ag (38) and Alox ( $\text{Al}_2\text{O}_3$ , 13).

Obviously, specimens that are heterogeneously composed of materials strongly different in density and atomic number require a careful X-ray analysis. Nevertheless, due to the irregular shape of the analyzed particles, the systematic error of EDX measurements is increased compared to that of a homogeneous specimen with flat and smooth surfaces. Commonly, the commercially available "standard less analysis software" are adjusted to 'ideally' smooth samples. Usually, the EDX analysis results are expressed in weight-percent (wt.%), in which the collected X-ray counts (intensity =  $f(\text{element conc.})$ ) will be converted into concentrations by means of an evaluation program taking into account fundamental X-ray parameters and the detector efficiency. The procedure is known as "standard less analysis" and is already established by the suppliers. To reduce errors resulting through different X-ray exit and scattering angles due to the different particle sizes, irregular dispersion, or agglomerated



catalyst deposits, a huge population of particles should be chosen for elemental analysis of bulk specimen. To obtain e.g. the amount of metal covering the support, data collection at low magnification as demonstrated in Fig.4. should preferably be performed.

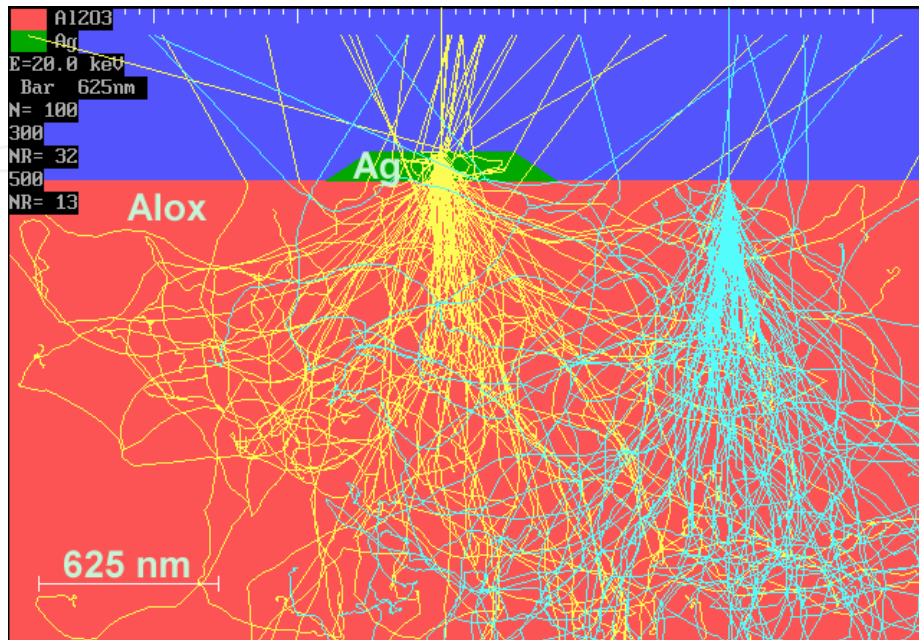


Fig. 3. MC simulation of electron trajectories created by a primary beam energy of 20 keV. Note the progress in the interaction volumes compared to Figure 2. N is equal to the number of used trajectories (100) for MC simulation. NR corresponds to the number of BS-electrons in case of Ag (32) and Alox ( $\text{Al}_2\text{O}_3$ , 13).

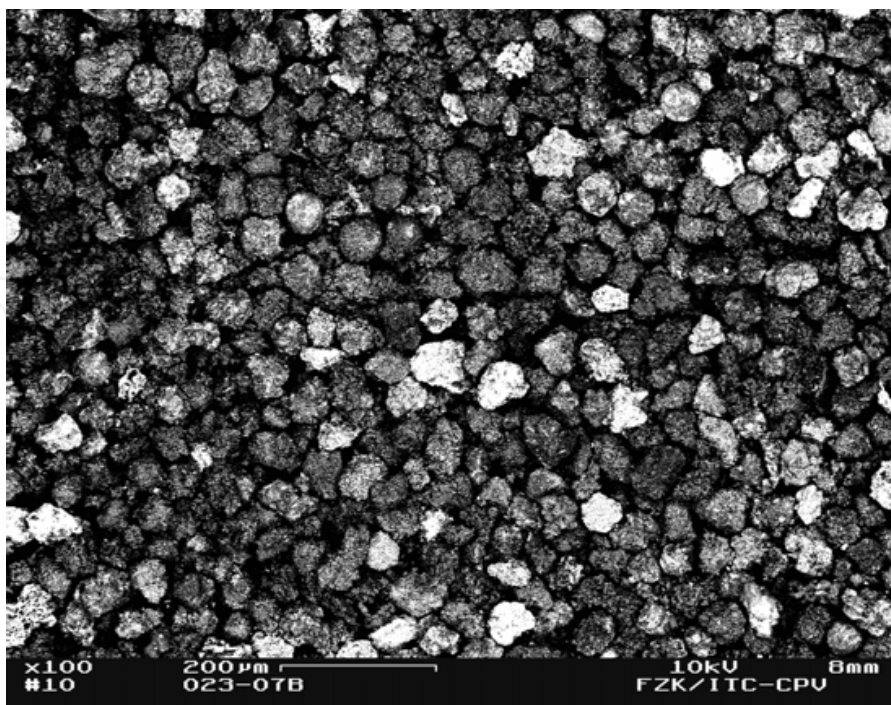


Fig. 4. Magnified (100 x) BSE image of a large population of  $\text{Al}_2\text{O}_3$  particles differently covered with Ag, prepared on a conventional specimen stub.

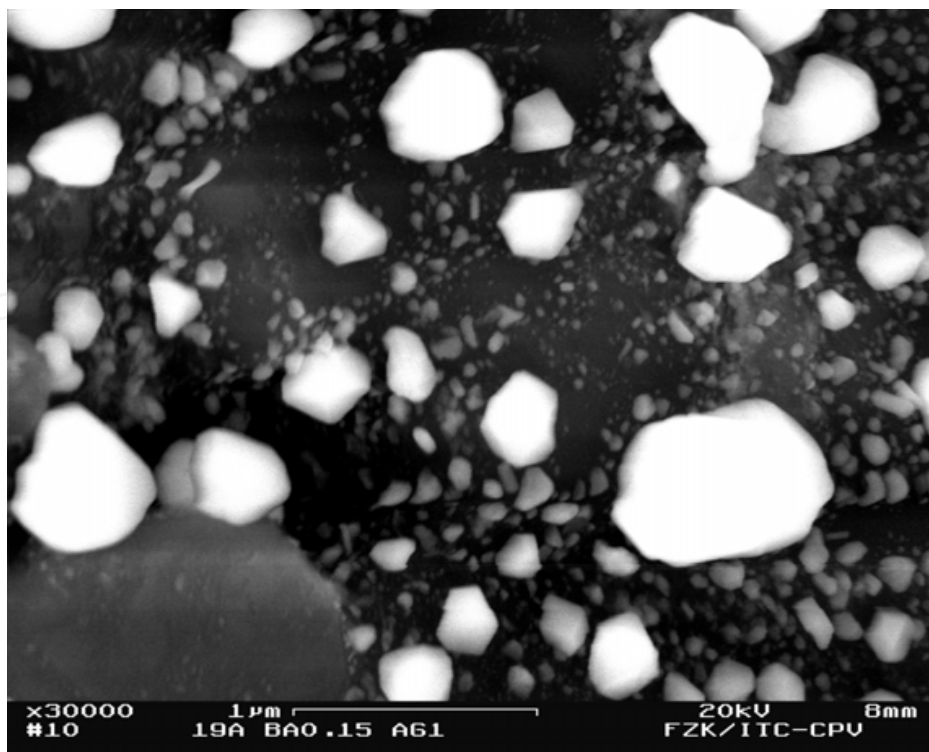


Fig. 5. High-magnification (30,000) image of a single  $\text{Al}_2\text{O}_3$  particle covered with different sized Ag clusters, prepared on a conventional specimen stub.

Therefore a great number of particles should be included in the analyzed region to average the influence of different shaped and sized particles. As an example, a low-magnified, large number of supporting alumina (Alox =  $\text{Al}_2\text{O}_3$ ) particles partially covered with Ag is shown in Figure 4 and produced under conditions mentioned in chapter 2.2. The magnification of 100  $\times$  is recommended for an EDX analysis to determine the amount of Ag deposited. The alumina particle diameter varies between 30  $\mu\text{m}$  and 80  $\mu\text{m}$ . For comparison, a highly magnified single alumina particle (sample D4) with differently sized and shaped Ag deposits is presented in Figure 5. It represents a high-magnification (30,000  $\times$ ) image of a single substrate particle, covered with differently sized Ag clusters. The size range of the deposited Ag is between 20 nm and 850 nm.

### 3.2 EDX line scans

Figure 6 shows an EDX line scan which is simulated by MC calculation using a bulk specimen geometry with an Ag deposit of 100 nm in thickness onto an alumina (Alox) support. It reveals the course of Ag-L $\alpha$ , Al-K $\alpha$  and O-K $\alpha$  X-rays across the specimen. The X-ray signals of Al and O dropped drastically down over the whole Ag cluster, contrarily the Ag signal becomes dominant. The lack in signal strength (intensity) is caused by absorption of the weak Al and O X-rays in the dense Ag particle. The maximum of the Ag signal, observed at the ends of the Ag deposit (edges) in the simulation is conspicuous. This is not observed in practice, only in the simulation.

Figure 7 is an example of an EDX line scan across the Ag agglomerate (approximately 620 nm) on a selected surface image of sample D6, which is generated by backscattered electrons. The line scan is shown in detail in Figure 8. One can see the pronounced

maximum of the Ag signal and the minimum of the Al signal, whereas the minimum of the O signal is less distinct as expected. It is a hint for the presence of subsurface oxygen or Ag bulk-dissolved oxygen, which will be discussed in chapter 3.6 in detail by means of O<sub>2</sub>-TPD and BET. The comparison between the experimental EDX line scan of sample D6 (Figure 8) and the simulated line scan (see Figure 6) is feasible.

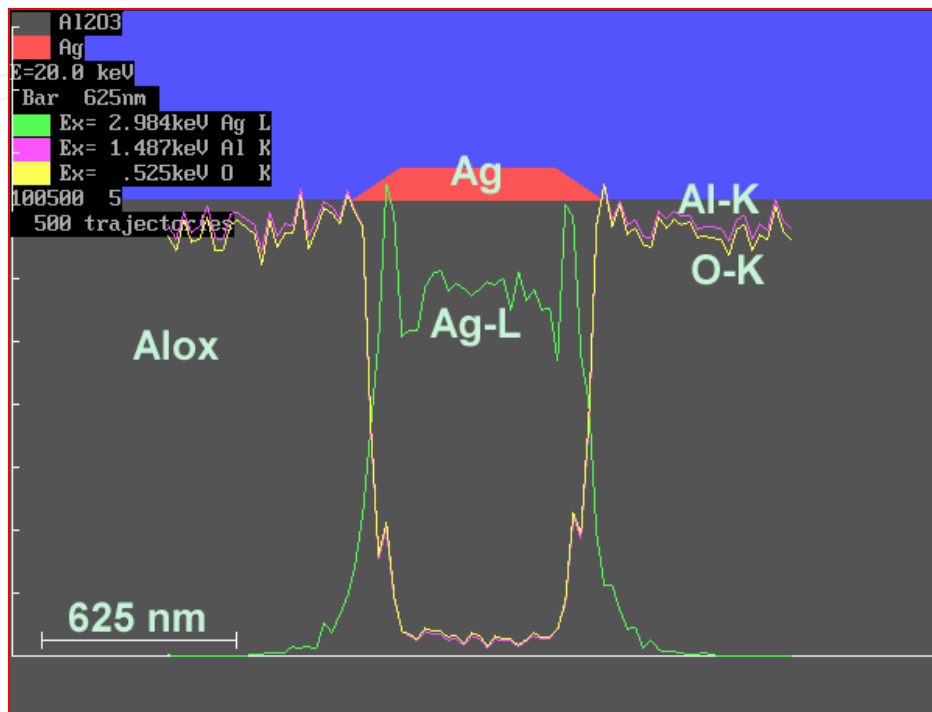


Fig. 6. MC simulation of an X-ray line scan (20 kV beam voltage) across a single particle deposited on an alumina (Alox) substrate.

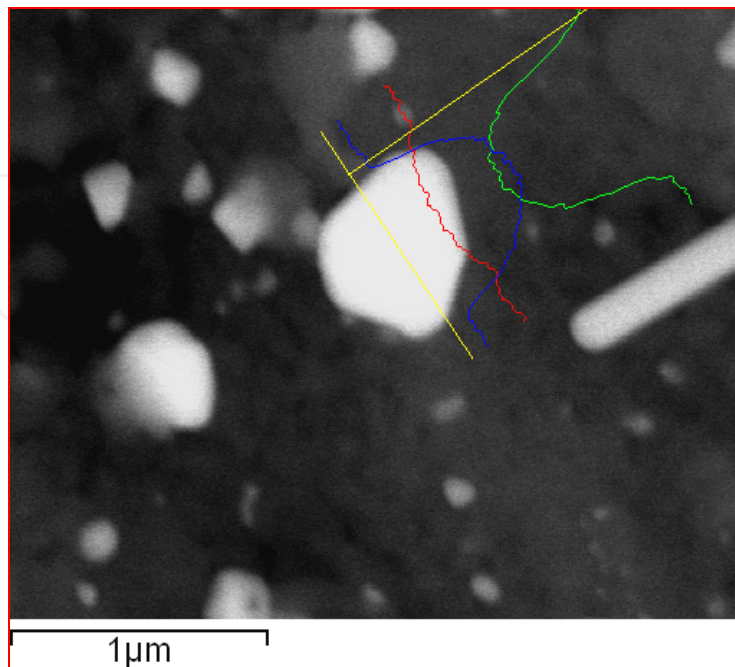


Fig. 7. BSE image of sample D6 and EDX line scan across a selected Ag deposit.

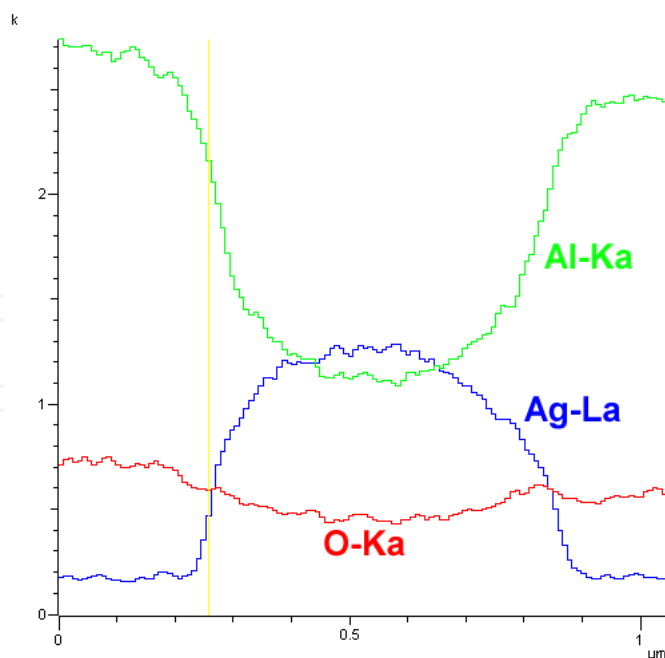


Fig. 8. Line scan in detail of Figure 7.

To demonstrate the imaging power of the T-SEM mode an example of a very tiny single alumina particle (D4) partially covered with Ag deposits in comparison to an extended particle (Figure 5) is shown in Figure 9. The dense Ag clusters appear as dark spots on the nearly "electron-transparent" alumina matrix. The graphical representation of an MC calculation based on an  $\text{Al}_2\text{O}_3$  (Alox) substrate of 92 nm in thickness and covered with a 20 nm thick Ag deposit on a TEM-grid support is depicted in Figure 10. It illustrates the transmitted electron trajectories with a strongly reduced excitation volume in contrast to Figure 3.

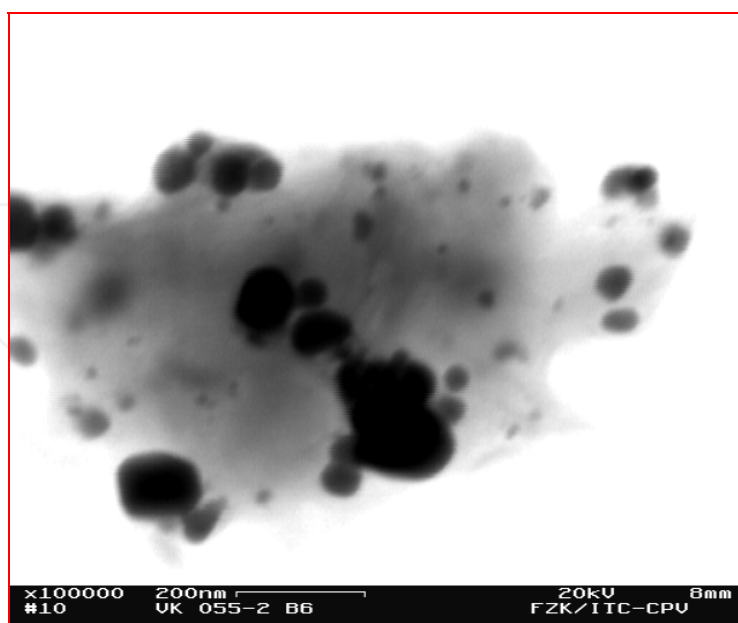


Fig. 9. Transmitted (TE) electron image (100,000  $\times$ ) of an irregularly shaped single alumina particle (light grey) partly covered with Ag clusters (dark), prepared on a TEM-grid support.

The MC simulation of the electron beam trajectories in Figure 10 and the X-ray line scan in Figure 11 visualizes the interaction of primary electrons with matter of different densities and thickness on a thin-film support. The broadening of the beam (skirt) depends on the specimen thickness and density.

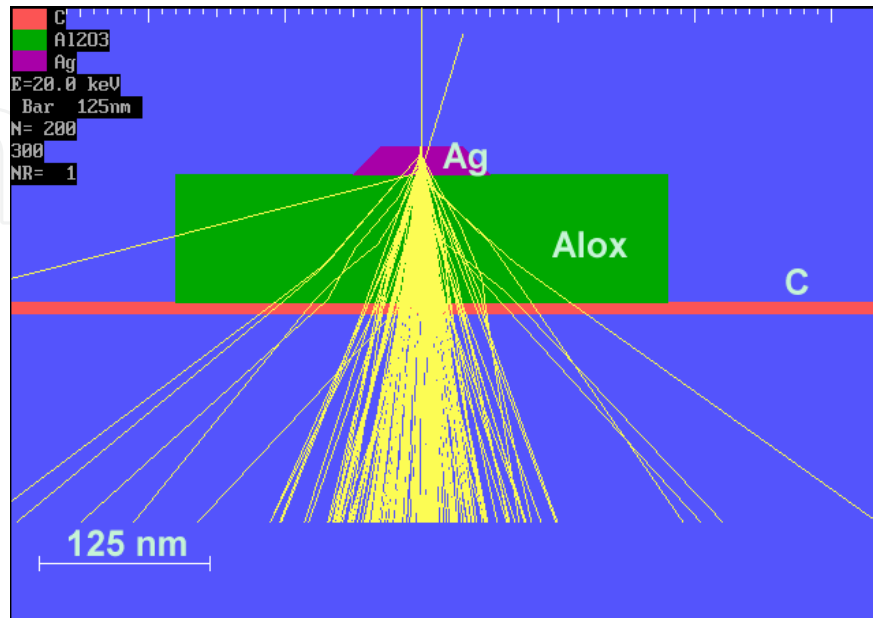


Fig. 10. MC simulation of the electron trajectories of an Ag deposit on an Alox (Al<sub>2</sub>O<sub>3</sub>) substrate, supported by an 8 nm carbon film (C) (TEM-grid). Note the broadening of the beam by passing the beam electrons through the matter. Backscattering events are drastically reduced (NR =1).

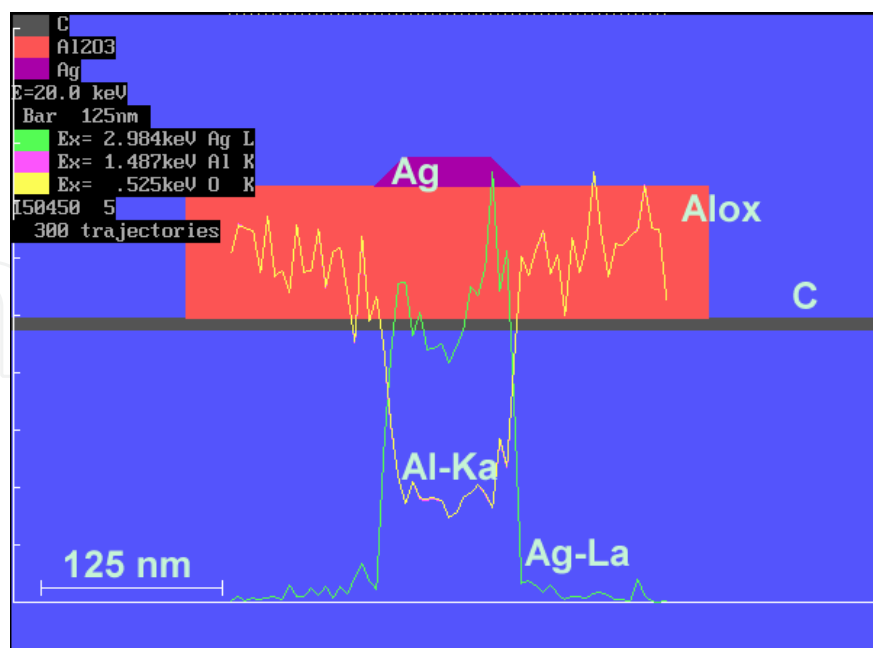


Fig. 11. X-ray line scan simulation of the thin film-supported (C) specimen. The course of the X-ray scan across the specimen is similar to that in Figure 6, but the intensity is decreased (indicated by the statistical fluctuations) due to the reduced beam interaction volume.



Thinner samples have better performance in resolution and contrast. In order to get highly magnified images even of tiny (sub nanometer) Ag particles, a TEM grid has to be prepared.

### 3.3 Ag distribution by EDX

In Figure 12 one can see the correlation of measured Ag concentration and the percentage of Ag area coverage visualized by image analysis (Figure 13). The image analysis is based on the intensity of the BSE signal.

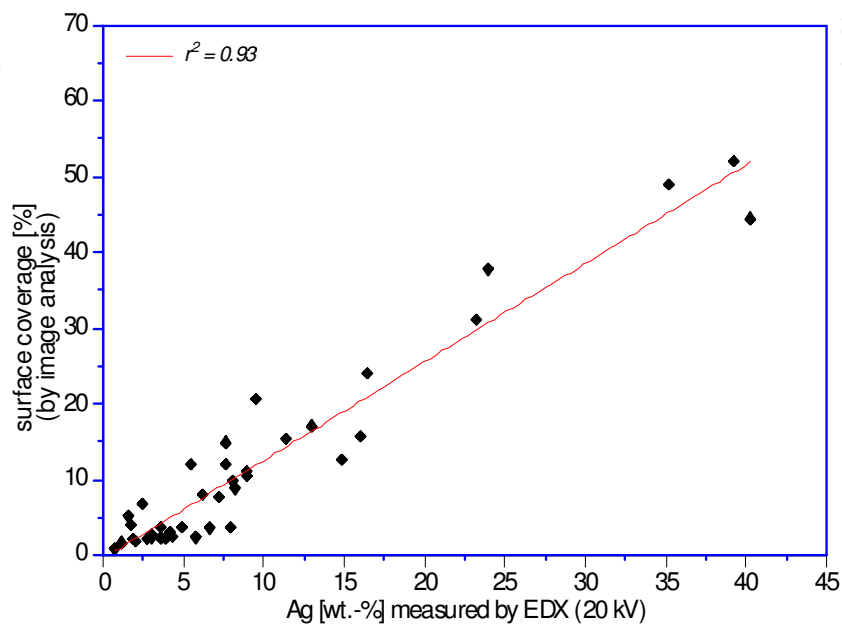


Fig. 12. Ag area coverage derived from the BSE signal and the correlation to the Ag concentration measured by EDX.

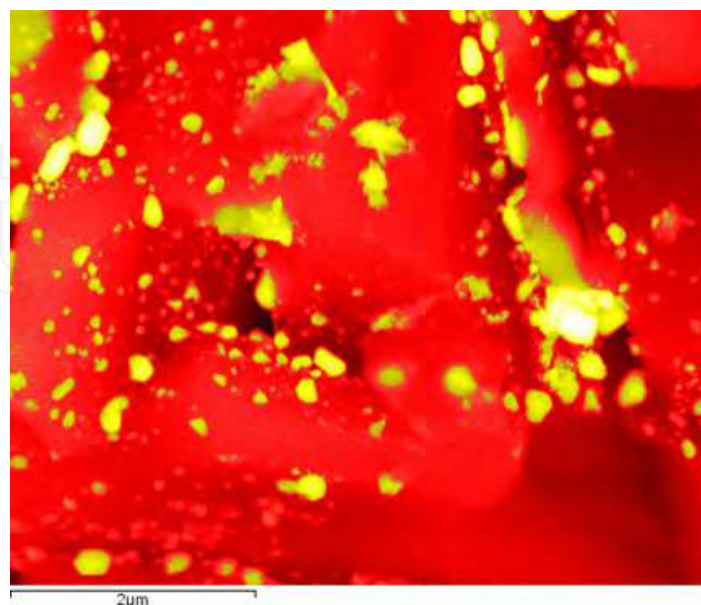


Fig. 13. Color rendering of a BSE image. The yellow areas represent Ag deposits. The red colored areas show the matrix ( $\text{Al}_2\text{O}_3$ ).



The yellow spots represent the Ag deposits, approximately 13.5% from the total area. It corresponds to approximately 11 wt.-% Ag measured by EDX. This procedure will not replace the numerical calculation by the evaluation program, but visualizes in a first approximation the dependence of the Ag concentration on the BSE contrast. The Ag distribution on the carrier material is discussed with regard to the penetration depth of primary beam electrons and lower limits of detection for X-ray analysis. It is crucial to catalytic activity that Ag particles cover the carrier material almost homogeneously. Sintering of Ag particles to Ag agglomerates has to be prevented [11]. Using sample D6 (20 % Ag / 1500 ppm Cs) as an example, the FESEM images (Figure 14) and EDX analysis results (Tab. 2) shall be discussed. The image reveals uniform grain sizes of the carrier material and variable coverage (bright areas) by Ag particles or Ag clusters. In the quadrants Q1, Q2, Q3, and Q4 of the SEM image of sample D6 the coverage of the carrier grains by Ag particles (Ag-clusters) varies (bright areas). The apparently uniform catalyst grains are assumed to result from the wet sieving of the carrier material (SLA92 and SC13). The EDX spectrum in Figure 15 reveals all significant elements Ag, Al, O, and Cs. Obviously, some of the grains are densely covered with Ag, others not. Figure 16 shows the shape of huge Ag agglomerates of the D6 sample in a higher magnification (30,000 x). There is no significant difference in the measured Ag surface content between the 4 quadrants in Figure 14, which indicates an "apparently homogeneous" distribution of Ag.

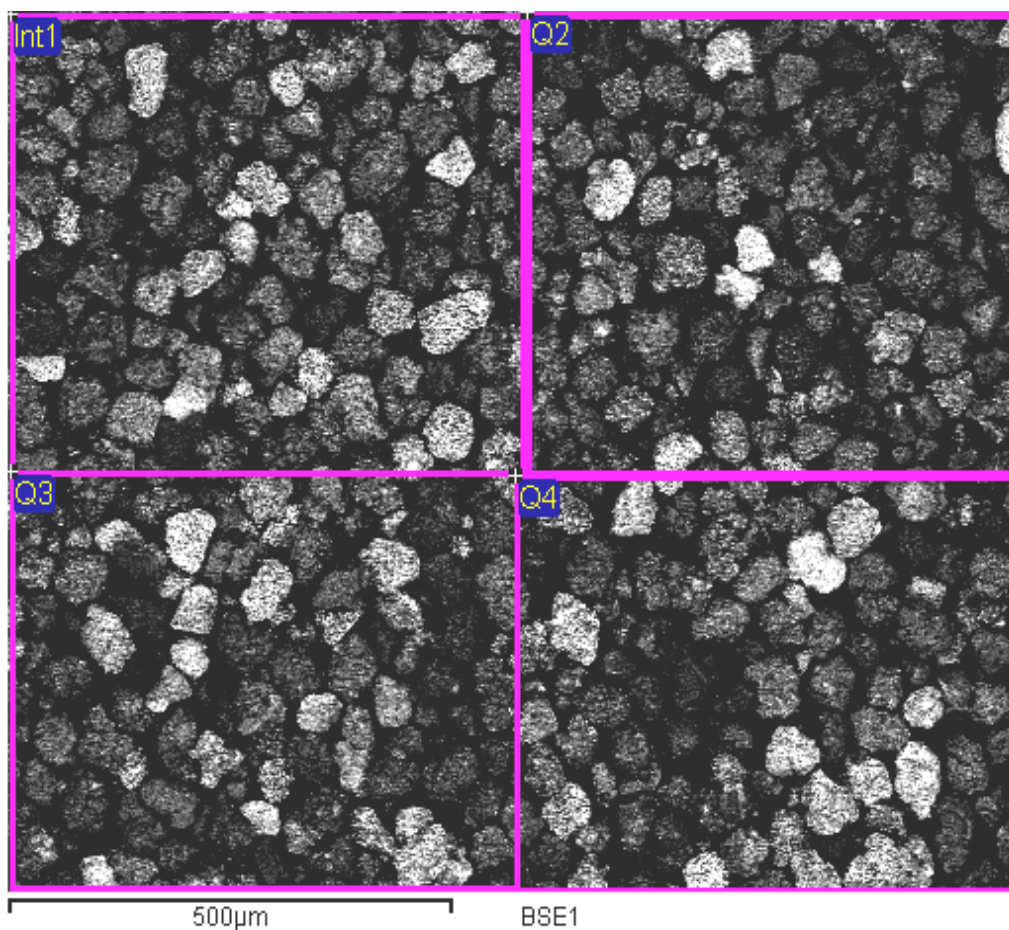


Fig. 14. SEM image of sample D6 (100 x, 20 kV) showing the 4 quadrants and the whole (integral) surface area analyzed by EDX (Tab.2).

EDX results sample D6	C	O	Al	Ag	Cs
Int1	3.0	51.8	29.8	15.1	0.12
Q1	2.6	51.3	30.2	15.9	0.00
Q2	5.4	51.2	30.3	13.1	0.00
Q3	1.9	52.2	30.6	15.2	0.15
Q4	3.1	51.4	29.1	16.4	0.00
average	3,3	51.6	30.0	15.1	0.01
standard deviation	1.3	0.40	0.60	1.30	0.07
max.	5.4	52.1	30.6	16.4	0.15
min.	1.9	51.2	29.1	13.1	0.00

Table 2. Results (wt %) of the EDX analysis of sample D6 shown in the FESEM image Figure 14 (100 x, 20 kV).

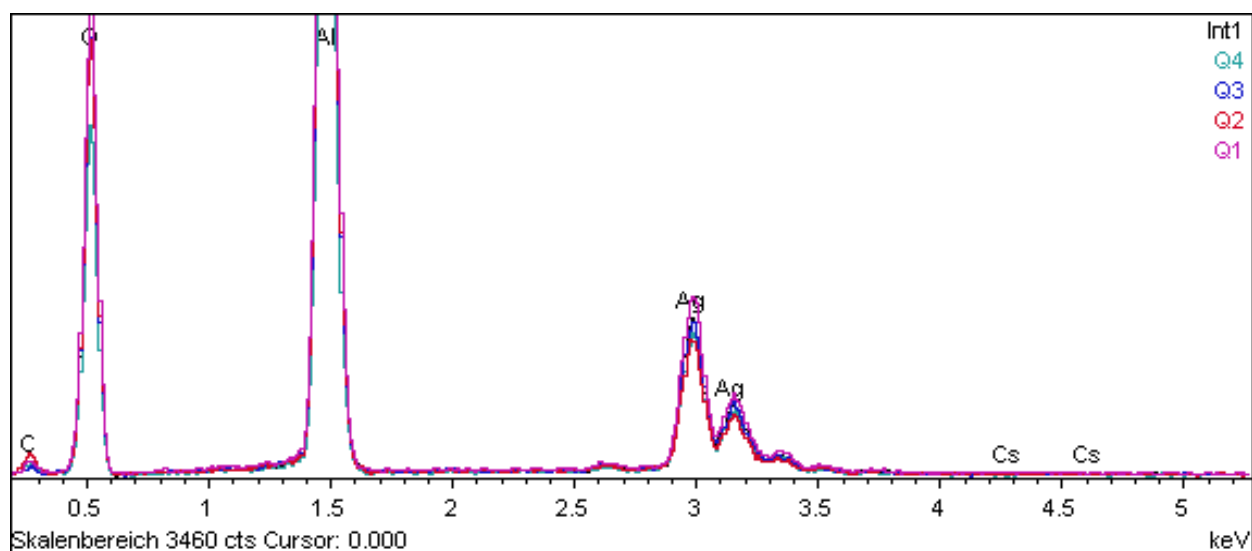


Fig. 15. EDX analysis of sample D6 (Figure 14) revealing Ag, Al, O, and Cs as significant elements.

According to Tab. 2, the average Ag concentration is 15.1% (average of Int1, Q1 to Q4) and the Ag concentrations in the quadrants do not vary significantly (Q1 = 15.9 % Ag, Q2 = 13.1 % Ag, Q3 = 15.2 % Ag, and Q4 = 16.4 % Ag). But the Ag concentrations doesn't correlate well with the absolute amounts of Ag (20 wt %) used for catalyst preparation. In general, the heterogeneous catalysts are influenced considerably by the penetration depth of the electron beam because of layer thickness, Ag cluster size, surface coverage, preparation performance and, under certain conditions, Ag bulk-dissolved oxygen (see chapter 3.6). Hence, the Ag values determined by EDX could differ from the absolute Ag concentrations of the prepared samples. The accuracy is strongly influenced by morphological effects and heterogeneity of the Ag coverage of the analyzed samples. Availability of reliable standards in this respect would be beneficial. In either case, for an absolute Ag determination a quantitative digestion should be carried out (4 wt% HF) and analyzed by ICP-AES (Inductive coupled plasma - atom emission spectroscopy) under appropriate conditions.

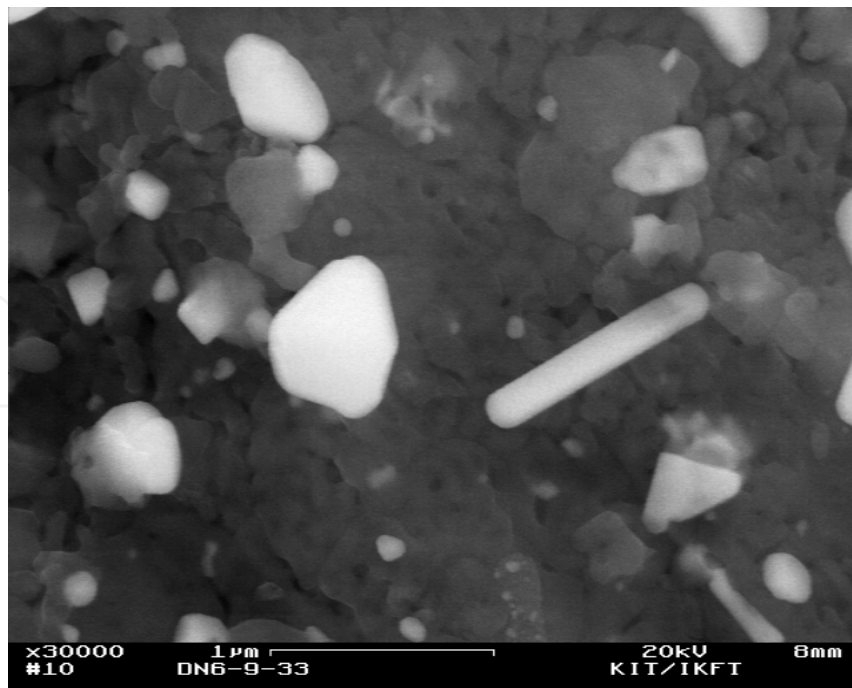


Fig. 16. Shape of huge Ag agglomerates of the D6 sample at 20 kV and 30,000 x.

### 3.4 EDX mapping

The dispersion of the Ag and Cs metal deposited on the catalyst support can also be characterized by the EDX mapping technique. Topographical and elemental imaging is possible at the same time. EDX mapping is a valuable tool to indicate the quality of the Ag dispersion. The electron beam is scanned pixel by pixel across a selected area of interest. In the following example, the element mappings for a selected specimen area (Figure 17, BSE image, bright spots indicating metal) revealed an inhomogeneous distribution of Ag (Figure 18) and Cs (Figure 19) of the catalyst support. Generally, the brighter the color appears, the higher is the concentration of the specific element. In both cases it correlates with the results in Tab. 3. Cs as a promoter facilitates Ag distribution on the  $\alpha$ - $\text{Al}_2\text{O}_3$  surface based on the high coverage and lack of crystallites with large contact angles [12]. The presence of Cs in the catalyst improves the distribution of Ag over the support and the Ag/Al interfacial area. Area P1 (see Figure 17 and Tab. 3), for instance, shows a remarkably high silver content of 66%, which is about twice as high as the average. The deviation from the average amount of Cs is not noticeable, because Cs is only present in small quantities (ppm). Nevertheless, the distribution of Ag and Cs can be shown very impressively by the time-consuming mapping. Spectra of the analyzed regions are shown in Figure 20. In summary it can be said that the inhomogeneity of metal distribution on the catalyst carrier material can be shown very clearly also for small amounts of metal. This example demonstrates a less quality of the preparation. One can see that the texture of the substrate SLA2 is very rough in comparison to SC31, which means that a homogeneous distribution of Ag and Cs is not so easy to achieve and requires an improvement in preparation. In case of an excellent preparation, this is a optimal Ag distribution for both catalyst systems, the question is which of the two catalyst systems is more favourable for the Ag-catalyzed epoxidation of 1,3-butadiene (1,3-BD) to 3,4-epoxy-1-butene (EpB) in the reactor.



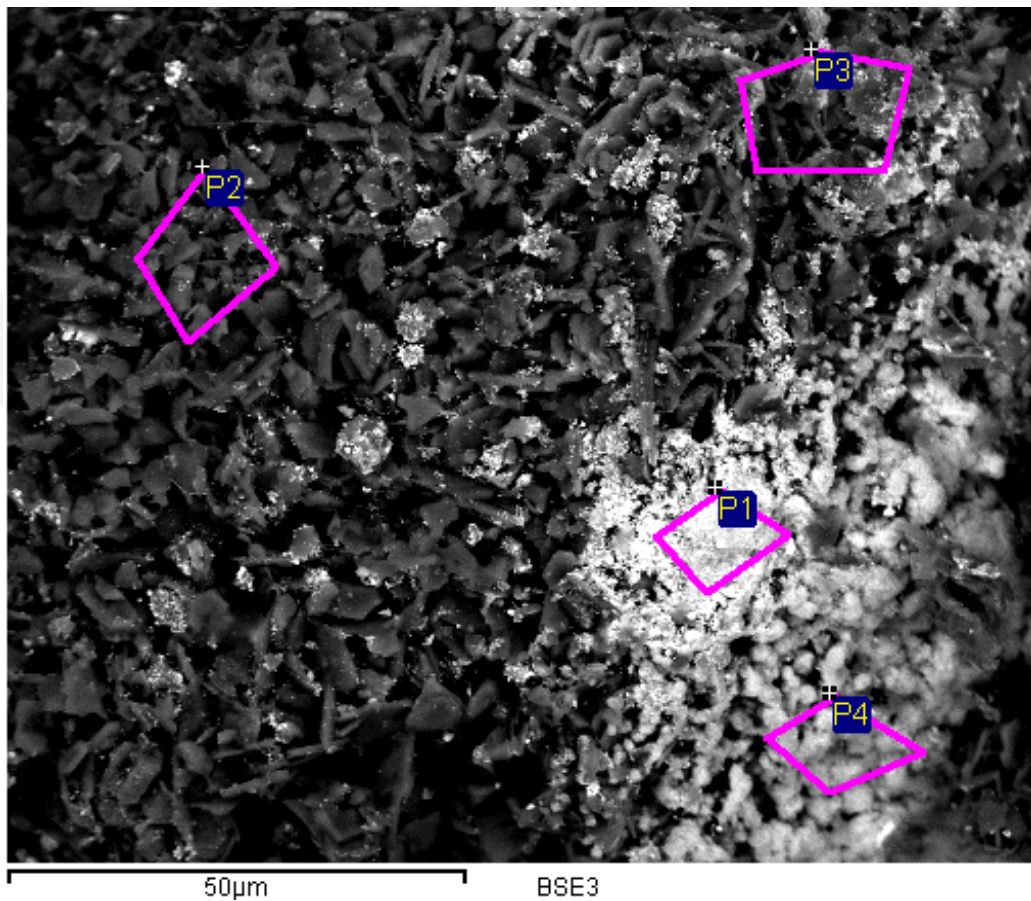


Fig. 17. BSE image of a selected area of an Ag catalyst particle (MZ06). The marked (red) areas P1, P2, P3 and P4 represent analyzed regions.

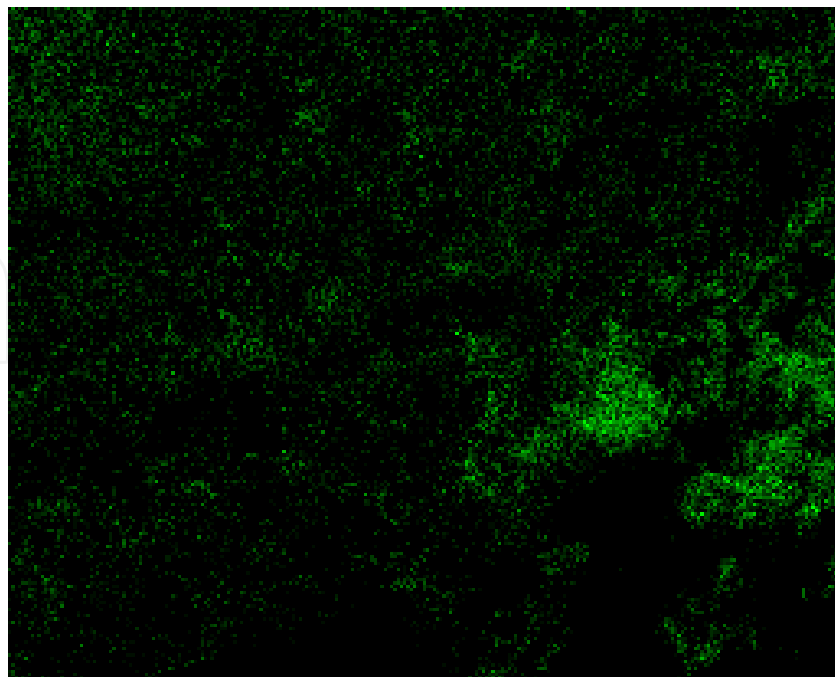


Fig. 18. Map of Ag-L $\alpha$  showing the inhomogeneous distribution of Ag. The Ag concentration correlates with the intensity of the green area (measuring time about 5 h).

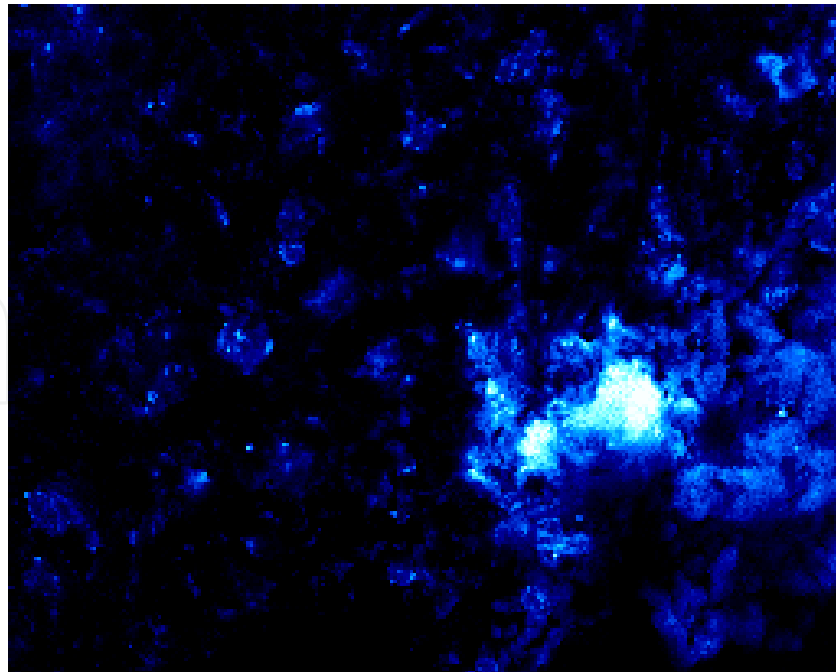


Fig. 19. Map of Cs-L $\alpha$  showing the inhomogeneous distribution of Cs. The Cs concentration is correlated with the intensity of the blue area (measuring time about 5 h).

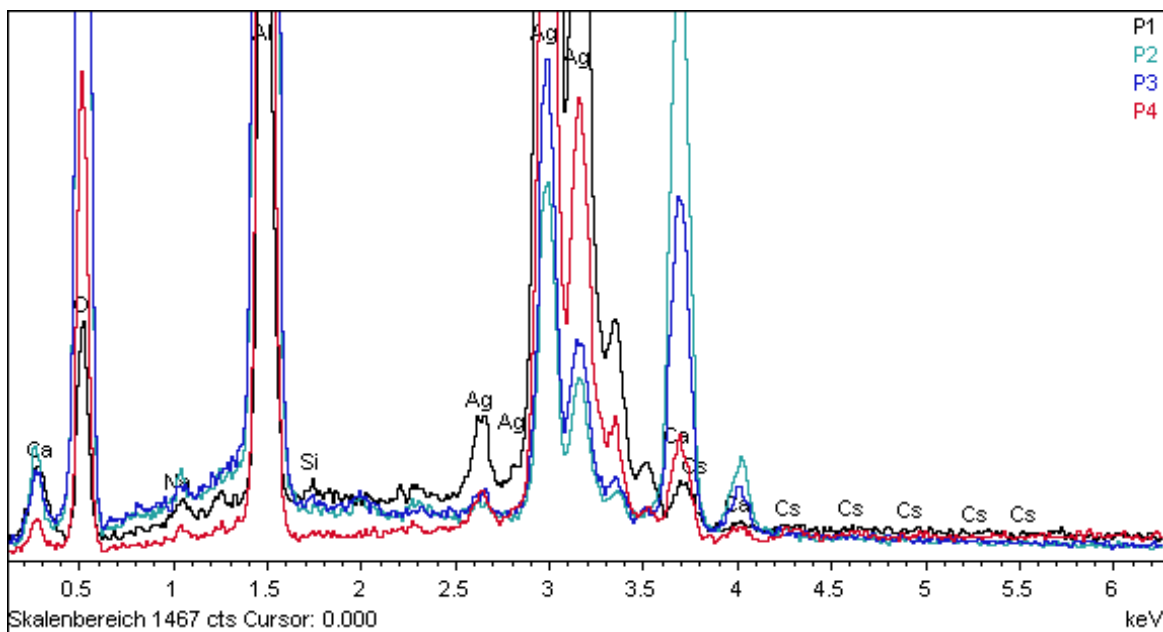


Fig. 20. Spectra of the analyzed regions (see Figure 17).

The rate of a catalyzed reaction should be proportional to the surface area of the active agent. Therefore it is desirable to have the active phase in form of the smallest possible particle. But the most undesired contribution to the reduction of the active surface (deactivation) is sintering (welding together of particles by applying heat below the melting point). The function of the support is to increase the active surface and to reduce the rate of sintering of the metal particles. On the other hand, the interaction between the lattice oxygen of the carriers and the metal particles also influences the behaviour of the active metal agent.

The support can modify the electronic character of the metal particle regarding to its adsorption and reactivity properties. Furthermore, the bond between the metal particle and the support can influence the shape of the metal particle (clusters). Both effects are so-called metal-support interactions (MSI). This effect decreases for supported Ag catalysts in the  $\text{SiO}_2 > \text{Al}_2\text{O}_3 > \text{C}$  sequence [2].

Spectrum	O	Na	Al	Si	Ca	Ag	Cs	Sum
P1	21.8	0.45	10.08	0.15	0.67	<b>66.33</b>	<b>0.45</b>	100
P2	54.1	0.32	31.16	0.00	6.62	<b>7.60</b>	<b>0.18</b>	100
P3	52.5	0.18	34.09	0.08	3.59	<b>9.53</b>	<b>0.00</b>	100
P4	38.6	0.28	19.59	0.04	2.16	<b>38.32</b>	<b>0.92</b>	100
average	41.8	0.31	23.73	0.07	3.26	<b>30.45</b>	<b>0.39</b>	100
max.	54.1	0.45	34.09	0.15	6.62	<b>66.33</b>	<b>0.92</b>	
min.	21.8	0.18	10.08	0.00	0.67	<b>7.60</b>	<b>0.00</b>	

Table 3. All results in wt.-%, derived from the BSE image in Figure 17.

Another tool to elucidate the distribution of elements is the so called CAMEO™ imaging. Figure 21 represents a CAMEO™ image from the examined specimen which is based on BSE detection. CAMEO™ is a tool to convert X-ray energies into visible wavelengths. In comparison to the X-ray mapping technique, the CAMEO™ procedure is much faster, but it may lead in some cases to a false color rendering (color overlap) caused by adjacent X-ray energies. As depicted in Figure 21 one can see that the brownish areas obscured the small Cs-spots. Therefore, Cs and Ag are not distinguishable because they are located at the same area of surface.

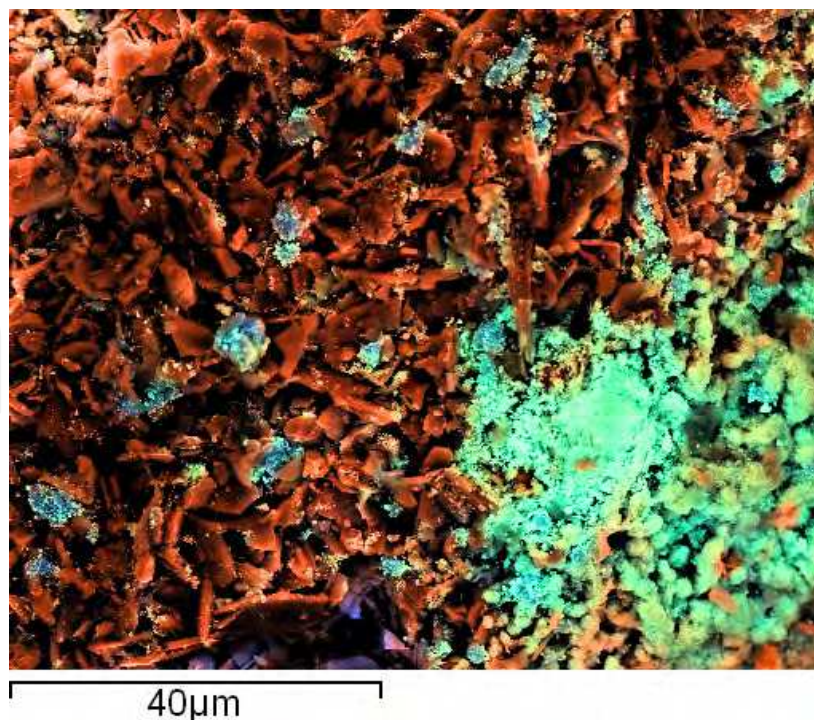


Fig. 21. CAMEO™ rendering of the area shown in Figure 17. The green colored areas represent Ag, whereas the brownish areas represent Al, respectively.



### 3.5 Remarks

All analytical results have been obtained at 20 kV acceleration voltages, which turned out to be the best choice for excitation conditions. Because the in-lens detector is switched off above 20kV, therefore high resolution SE imaging is disabled. The EDX results are determined by the manufacturer's spectrum evaluation software (Oxford corp.). Originally, all quantitative results are calculated with two significant fractional decimal digits provided with  $1\sigma$  errors, which includes the errors resulting from spectra processing (background subtraction, filtered least squares fitting, peak overlap). Notably, this may not reflect uncertainties caused by surface topography and other systematic influences. According to experience, the actual uncertainties are considerably higher, especially for light elements. We suggest for C and O a relative uncertainty of 5 - 20%, for all other elements 1-5% [13]. Another important issue is the estimation of the *limit of detection* (LOD), which can be calculated from a synthetic spectrum by the equation 2.

$$LOD_{3\sigma} = 3 \cdot \sqrt{B} \cdot \frac{C}{P} \quad (2)$$

Where B is the number of background counts,  $3 \cdot B^{1/2}$  represents  $3\sigma$  error of background measurement, C is the concentration of the element, P corresponds to the number of counts in the X-ray line after background subtraction. In practice, calculation will be performed by a special program tool named '*spectrum synthesis*', which is provided with the INCA-Energy evaluation software [14].

LOD $3\sigma$ / w t.- %		I / nA	$t_m$ / s	U / kV
Ag	Cs			
0.21	-	0.23	60	20
0.18	0.27	0.23	100	20
0.09	0.15	0.71	100	20
0.06	0.09	0.71	300	20

Table 4. Calculated  $3\sigma$  LOD's regarding to equation 2 and [14]. The matrix composition, except for alumina, is assumed to be 1.8 wt.-% Ca, 0.3 wt.-% Na, 0.2 wt.-% P.

For the  $3\sigma$  LOD estimation, the composition of the sample matrix and the acquisition parameters like measuring time  $t_m$ , beam voltage U, current I, detector parameters, X-ray take-off angle are required. Tab. 4 shows  $3\sigma$  LOD's which are calculated for 3 different measuring times and aperture adjustments (beam current). For Ag, this is of minor importance, since the amounts of Ag are sufficiently high in comparison to the promoters. The pore size of the alumina support is in a similar order of magnitude as the X-ray generating range (see Fig. 1b), which leads to an uncertainty in the measurements in these regions. As a consequence, the EDX analysis is considered to be semi-quantitative on such  $Al_2O_3$  supports. A loss of X-rays (Al-K $\alpha$  and O-K $\alpha$ ) emitted from mesoporous media compared to that of dense monocrystalline alumina is described in literature [15]. It may be

caused by charge effects due to the specific surface of particles and distribution of pores. In the course of our various measurements, no significant charging was observed. Compared to common *inductively coupled plasma atomic emission spectroscopy* (ICP-AES) the values of metal deposition determined by EDX are frequently higher. One explanation is a sometimes observable incomplete chemical digestion prior to ICP measurements. In the case of  $\text{Al}_2\text{O}_3$  we recommend a digestion with HF (4%). As already mentioned, EDX with an electron penetration depth in the order of several nanometers up to microns is a technique for surface analysis, while the ICP technique is applicable to the quantitative determination of the bulk composition with the detection limits in the  $\mu\text{g}/\text{l}$  (ppb) range. Due to the incipient wetness impregnation technique applied here for surface preparation, the values of metal deposition analyzed by EDX are expected to be higher than those by ICP-AES [16]. The differences in the amounts of Ag are plausible. The reason therefore is that the D-samples and MZ-samples are completely chemically digested, which is a physical homogenization. In contrast, the sample preparation for FESEM/EDX is non-destructive, which means that the sample is not physically homogenized. Tab. 5 gives a selected overview about catalysts characterization methods applied on sample D1.

Promoter $\text{CsNO}_3$ / wt.-%	ICP Ag / wt.-%	EDX Ag / wt.-%	BET $\text{m}^2\text{g}^{-1}$
0.15	4.46	5.76	6.03

Table 5. A listing of commonly applied laboratory methods (ICP, EDX, BET) for characterization of a catalyst with nominal 5 wt.-% Ag, grain fraction 45-63  $\mu\text{m}$  (sample D1).

### 3.6 $\text{O}_2$ -TPD and BET measurement

To get a deeper insight it makes sense to combine SEM with  $\text{O}_2$ -TPD experiments and BET measurements, which additionally were carried out. The TPD experiment measures the temperature-dependent desorption rate of a molecule from the catalyst surface [17]. Typically,  $\text{O}_2$  / Ag interactions are studied on the Ag monocrystal surfaces (110) and (111) [18]. This means that silver may storage  $\text{O}_2$ , with the amount adsorbed being dependent on temperature and  $\text{O}_2$  partial pressure.  $\text{O}_2$  dissociatively adsorbs on the Ag catalyst and may assume the following characteristic forms:

- Surface oxygen
- Subsurface oxygen
- Ag bulk-dissolved oxygen

Ag bulk-dissolved oxygen may act as a storage of converted surface oxygen and, hence, be supplied later on. Subsurface  $\text{O}_2$  increases the coordination number of Ag surface atoms, which results in a smaller binding strength of surface oxygen and favourably influences the epoxidation reaction of 1,3-BD. The surface area has been corrected by the subsurface oxygen value. Comparison of the measured amount of  $\text{O}_2$  desorbed with the amount theoretically required for an  $\text{O}_2$  monolayer shows that the measured amount of desorbed  $\text{O}_2$  is higher by a factor of 2. This may be explained by the presence of subsurface  $\text{O}_2$  [19].

O<sub>2</sub>-TPD studies reveal significant differences between MZ samples with an SLA92 carrier and D samples with an SC13 carrier for the same Ag contents. In general it can be said that the desorbed O<sub>2</sub> amounts of the MZ samples are below those of the D samples by a factor of 5. Moreover, the temperatures of the desorption maximums of the MZ samples are lower. This difference (binding strength of oxygen) results in a strongly variable reactivity of the adsorbed oxygen species. Figure 22 shows O<sub>2</sub> desorption and temperature of the samples D1, D3, and D5 with different Ag concentration on the support that is *not doped with Cs*. With increasing Ag concentration, the desorption maxima are shifted towards lower temperatures (red line). This indicates that epoxidation already may start at lower temperatures. Figure 23 shows that the sample D6 doped with Cs reaches a higher temperature at the desorption maximum than the non-doped sample D5.

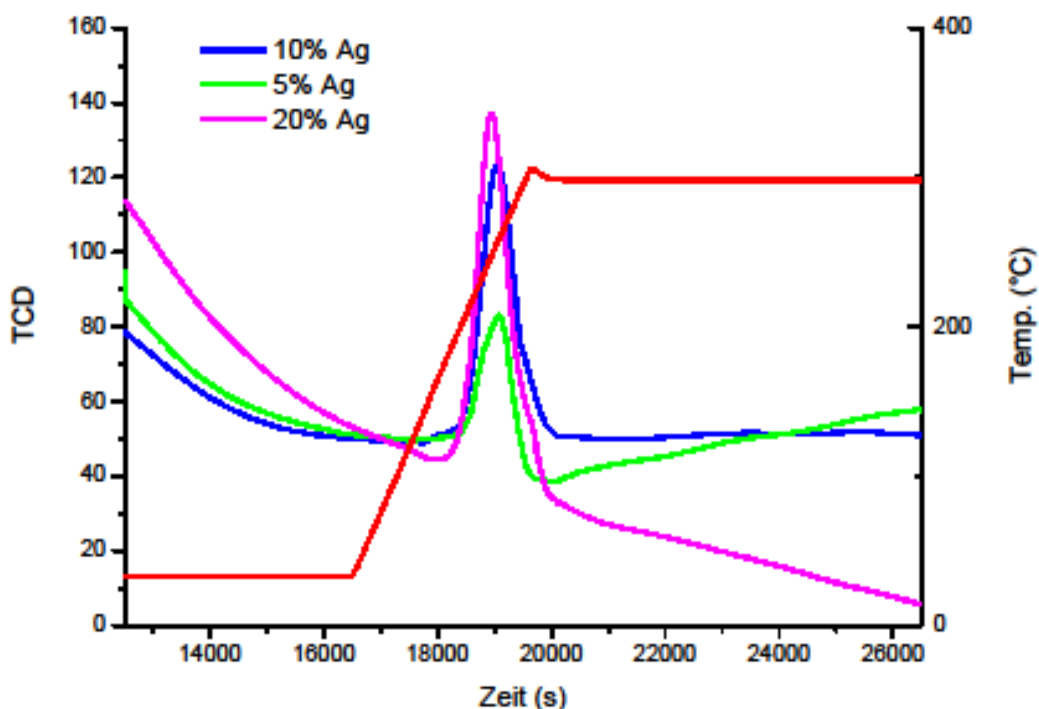


Fig. 22. O<sub>2</sub> detection (WLD) by O<sub>2</sub>-TPD of the samples D1 (5 % Ag), D3 (10 % Ag), and D5 (20 % Ag) versus temperature (red line).

This indicates that the adsorbate is stabilized by the presence and the grade of distribution of Cs and Ag on the surface, which correlates with TPD results, FESEM, EDX mapping and the reaction performance. The determination of the specific surface areas of the catalysts D3, D4, D5, D6, MZ06 and MZ09 gives an important hint regarding to metal distribution of MSI effects. Tab. 6 lists the specific surface areas for the mentioned catalysts determined with N<sub>2</sub> as adsorptive. All isotherms are of the IUPAC type II (“s-shaped”) and, hence, can be evaluated according to the BET theory [20], [21]. The Cs-doped samples (D4, D6) have a slightly higher surface than the non-doped samples (D3, D5) with the same Ag content, which correlates to a higher desorption rate for O<sub>2</sub>-TPD. In case of the samples MZ06 and MZ09 one can see that the difference in BET surface is not remarkable, even in the presence of different Ag amounts. The total error for BET measurement is about 0.1 m<sup>2</sup>/g.

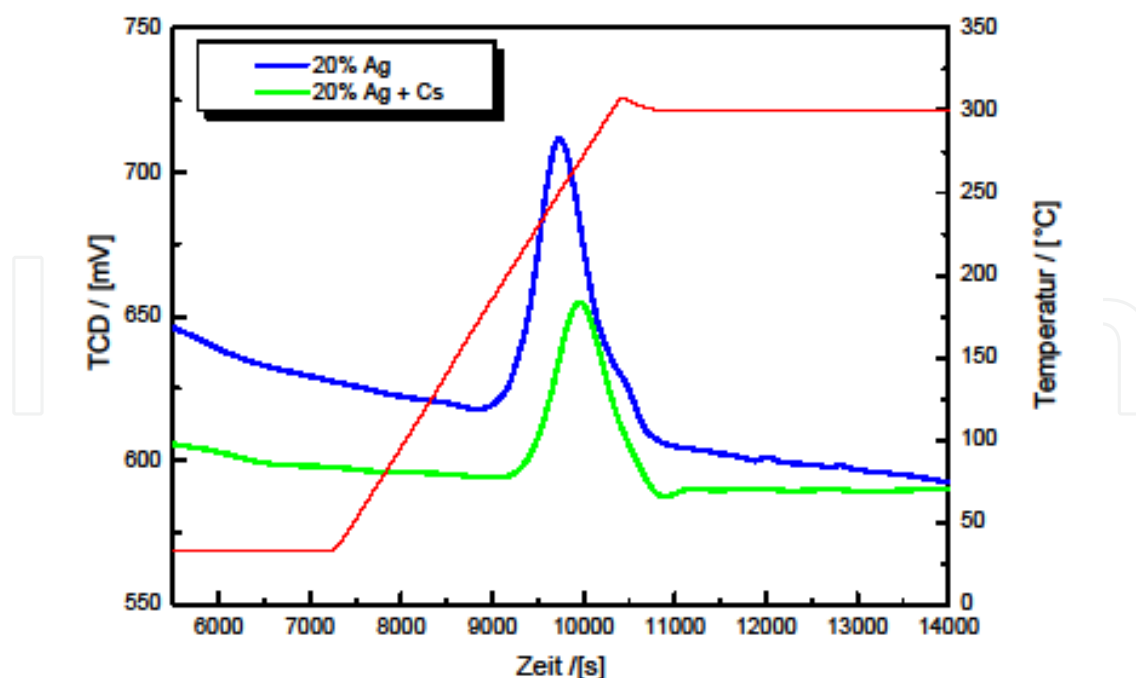


Fig. 23. O<sub>2</sub> detection (WLD) by O<sub>2</sub>-TPD of samples D5 (20 % Ag) and D6 (20 % Ag + Cs) versus temperature (red line).

	D3	D4	D5	D6	MZ06	MZ09
	Ag 10%	Ag 10% + Cs	Ag 20%	Ag 20% + Cs	Ag 5% + Cs	Ag 10% + Cs
$a_{s,BET}$ [m <sup>2</sup> g <sup>-1</sup> ]	6,0424	6,5521	7,6083	8,0461	0,80722	0,7009

Table 6. Specific surface areas from sample D3 – D6 and MZ06 and MZ09.

The BET reveals that there is a significant difference in the catalyst surface, which is expressed by the topological images of FESEM of the D samples (SC31) and MZ (SLA92) samples. Note: Very small amounts (0,1g) of sample are used for the investigations (FESEM, TPD). In the case of BET-Measurement the sample weight is in the range of 0.1 g up to 10 g, depending on the specific surface. The carrier material SC13 (high BET Surface) was not found to be suited for the epoxidation of 1,3-butadiene (Figure 24) on Ag particles. Already at 180°C a total oxidation of 1,3-butadiene to CO<sub>2</sub> and H<sub>2</sub>O does occur, also when Cs-doped catalysts are used. In contrast to this, epoxidation of the Ag catalyst with SLA29 (less BET surface) carrier material results in an EpB selectivity of 74 % (200° C, SV = 2590 h<sup>-1</sup>) at a 1,3-BD conversion rate of 15 % [22]. The constitution of the oxametallacycle intermediate is depicted in Figure 25. The guiding hypothesis is that surface oxametallacycles are key intermediate for epoxidation on Ag / Cs catalysts. The intermediate EpB(ads), finally leading to molecular EpB, is probably strongly adsorbed on the catalyst surface indicated by theoretical calculations which also support its identity as an oxametallacycle. The oxametallacycle intermediate is more thermodynamically stable than EpB by approx. 24 kcal/mol. Moreover, the transition state for EpB formation from the oxametallacycle intermediate is actually lower in energy than the reactants, butadiene and oxygen [23].

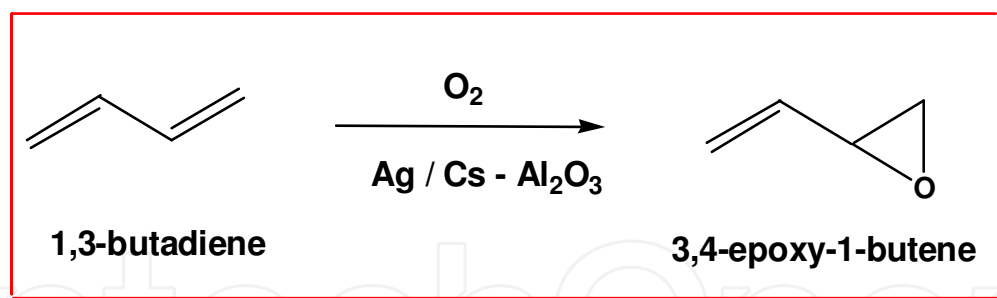


Fig. 24. Epoxidation of 1,3-butadiene over Ag / Cs catalyst on  $\text{Al}_2\text{O}_3$  to 3,4-epoxy-1-butene.

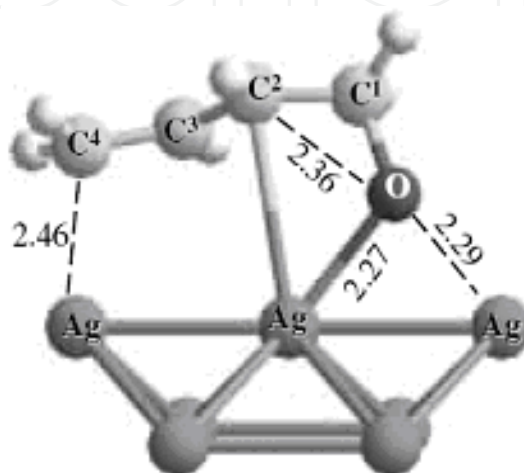


Fig. 25. The "intermediate EpB" finally leading to molecular EpB. The oxametallacycle intermediate is more thermodynamically stable than EpB. Moreover, the transition state for EpB formation from the oxametallacycle intermediate is actually lower in energy than the reactants, butadiene and oxygen

#### 4. Conclusions and outlook

Production of Ag catalysts based on a corundum-containing (SC13) and a calcium hexa aluminate-containing (SLA92) carrier material is crucial to the selective epoxidation of 1,3-butadiene. Optimum distribution and morphology of the Ag particles must be ensured by controlled, tailored catalyst synthesis. An increase in the activity by enhanced Ag dispersion on a corundum-containing carrier material with a larger surface area leads to completely unselective catalysts. FESEM/EDX results provide major information with regard to the Ag distribution and the properties of the carrier surfaces. The carrier material SC13 was not found to be suited for the epoxidation of 1,3-butadiene on Ag particles. At 180°C already does a total oxidation of 1,3-butadiene to  $\text{CO}_2$  and  $\text{H}_2\text{O}$  occur also when Cs-doped catalysts are used. In contrast to this, epoxidation of the Ag catalyst with SLA29 carrier material results in an EpB selectivity of 74 % (200 °C,  $\text{SV} = 2590 \text{ h}^{-1}$ ) at a 1,3-BD conversion rate of 15 %. All the analysis methods complement each other to form an overall impression, which is reflected in the product selectivity, catalyst activity and educts conversion during the reaction. The distribution and composition of metal particles on the surfaces can be seen and detected with EDX and FESEM. Also topological and morphological effects can be shown. BET measurements allow drawing a conclusion for successful metal loading. Furthermore,



the efficiency of Ag-loading and promoters with TPD measurements can be determined. The analytical result reflects the final behaviour of the epoxidation regarding to the product selectivity and conversion rate of the educts.

## 5. Acknowledgement

Doreen Neumann-Walter, (preparation), KIT, Germany  
Bernhard Powietzka, (preparation, reaction control), KIT, Germany  
Sara Essig, (preparation), KIT, Germany  
Dr. Angela Puls, (BET measurement), Rubotherm GmbH Bochum, Germany  
Dr. Volker Hagen (O<sub>2</sub>-TPD measurement), Rubokat GmbH Bochum, Germany

## 6. References

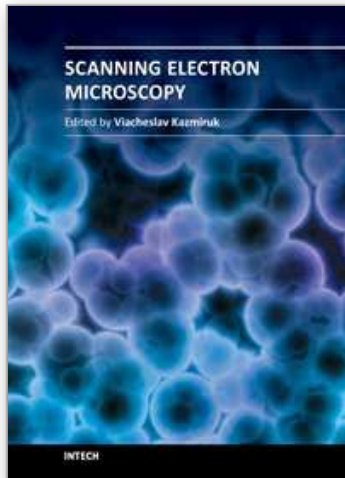
- [1] R. J. Wijngaarden, A. Kronberg, K. R. Westerterp, *Industrial Catalysis*, WILEY-VCH Verlag GmbH Weinheim, 1998
- [2] B. Cornils, W. A. Hermann, R. Schlögl, Chi-Huey Wong, *Catalysis from A to Z*, WILEY-VCH Verlag GmbH, 2000
- [3] J. R. Monnier, *Prepr. Pap. - Am. Chem. Soc., Div. Fuel Chem.* 2007, 52 (2), 163
- [4] M. Pohl, S. Hoge Kamp, N. Q. Hoffmann, H. P. Schuchmann, *Chem. Ing. Tech.* 2004, 76 (4), 392
- [5] J. M. Thomas, R. M. Lambert (Ed.), *Characterisation of Catalysts*, Chichester, Wiley 1980
- [6] P. L. Gai, E. D. Boyes, *Electron Microscopy in Heterogeneous Catalysis*, Inst. of Physics Publishing, Bristol and Philadelphia, 2003
- [7] W. Habicht, N. Boukis, G. Franz, O. Walter, E. Dinjus, *Microsc. Microanal.* 2006, 12, 322-326
- [8] C. E. Lyman et al.; *Scanning Electron Microscopy, X-ray Microanalysis, Analytical Electron Microscopy: a Laboratory Workbook*; Plenum Press N. Y. (1990)
- [9] L. Reimer, *Monte Carlo Simulation of Electron Diffusion*, updated Version 3.1, Program and Handbook, Münster, Germany 1998
- [10] J. I. Goldstein et al., *Scanning Electron Microscopy and X-ray Microanalysis*, 3<sup>rd</sup> ed., Kluwer Academic/Plenum Publishers, New York, 2003
- [11] *Handbook of Heterogeneous Catalysis*, Vol.1, 2nd Ed. (Eds: G. Ertl, H. Knözinger, F. Schüth, J. Weitkamp) Wiley-VCH, Weinheim 2008, 561
- [12] D. M. Minahan, G. B. Hoflund, W. S. Epling, D. W. Schoenfeld, *J. of Catalysis* 168, 1997, 393-399
- [13] W. Habicht, N. Boukis, E. Hauer, E. Dinjus, *X-ray Spectrometry* 2011, 40, 69-73
- [14] INCA Energy, tools for INCA users, provided by Oxford corp., or more profound: P. Duncumb, I. R. Barkshire, P. J. Statham, *Microsc. Microanal.* 2001, 7, 341-355
- [15] L. Sorbier, E. Rosenberg, C. Merlet, X. Llovet, *Mikrochim. Acta*, 2000, 132, 189-199
- [16] C. Xu, J. Zhu, *Nanotechnology* 2004, 15, 1671-1681
- [17] M.I. Szykoska, E. Lesniewska, T. Paryjczak, *Pol. J. Chem.* 2003, 77, 657
- [18] F. M. Leibsle et al., *Phys. Rev. Lett.* 1994, 72, 569, 569-2572.
- [19] G.W. Busser, O. Hinrichsen, M. Muhler, *Cata. Lett.* 2002, 79 (1 - 4), 49



- [20] D. D. Do, *Adsorption Analysis: Equilibria and Kinetics*, Imperial College Press, London 1998
- [21] P. Christopher and S. Linic, *ChemCatChem* 2010, (1), 2, 78
- [22] T. N. Otto, P. Pfeifer, S. Pitter, B. Powietzka, *Chem. Ing. Tech.* 2009, 81 (3), 349
- [23] Mark A. Barteau, *Topics in Catalysis* Vol. 22, Nos. 1/2, January 2003

IntechOpen

IntechOpen



## **Scanning Electron Microscopy**

Edited by Dr. Viacheslav Kazmiruk

ISBN 978-953-51-0092-8

Hard cover, 830 pages

**Publisher** InTech

**Published online** 09, March, 2012

**Published in print edition** March, 2012

Today, an individual would be hard-pressed to find any science field that does not employ methods and instruments based on the use of fine focused electron and ion beams. Well instrumented and supplemented with advanced methods and techniques, SEMs provide possibilities not only of surface imaging but quantitative measurement of object topologies, local electrophysical characteristics of semiconductor structures and performing elemental analysis. Moreover, a fine focused e-beam is widely used for the creation of micro and nanostructures. The book's approach covers both theoretical and practical issues related to scanning electron microscopy. The book has 41 chapters, divided into six sections: Instrumentation, Methodology, Biology, Medicine, Material Science, Nanostructured Materials for Electronic Industry, Thin Films, Membranes, Ceramic, Geoscience, and Mineralogy. Each chapter, written by different authors, is a complete work which presupposes that readers have some background knowledge on the subject.

### **How to reference**

In order to correctly reference this scholarly work, feel free to copy and paste the following:

Thomas N. Otto, Wilhelm Habicht, Eckhard Dinjus and Michael Zimmerman (2012). Catalyst Characterization with FESEM/EDX by the Example of Silver-Catalyzed Epoxidation of 1,3-Butadiene, Scanning Electron Microscopy, Dr. Viacheslav Kazmiruk (Ed.), ISBN: 978-953-51-0092-8, InTech, Available from: <http://www.intechopen.com/books/scanning-electron-microscopy/catalyst-characterization-with-fesem-edx-by-the-example-of-the-epoxidation-of-1-3-butadiene->

**INTECH**  
open science | open minds

### **InTech Europe**

University Campus STeP Ri  
Slavka Krautzeka 83/A  
51000 Rijeka, Croatia  
Phone: +385 (51) 770 447  
Fax: +385 (51) 686 166  
[www.intechopen.com](http://www.intechopen.com)

### **InTech China**

Unit 405, Office Block, Hotel Equatorial Shanghai  
No.65, Yan An Road (West), Shanghai, 200040, China  
中国上海市延安西路65号上海国际贵都大饭店办公楼405单元  
Phone: +86-21-62489820  
Fax: +86-21-62489821

© 2012 The Author(s). Licensee IntechOpen. This is an open access article distributed under the terms of the [Creative Commons Attribution 3.0 License](#), which permits unrestricted use, distribution, and reproduction in any medium, provided the original work is properly cited.

IntechOpen

IntechOpen